Linked topological colloids in a nematic host

Angel Martinez[a,b], Leonardo Hermosillo[a], Mykola Tasinkevych[c,d], and Ivan I. Smalyukh[a,b,e,f,1]

[a]Department of Physics, University of Colorado Boulder, Boulder, CO 80309; [b]Theory of Inhomogeneous Condensed Matte, Liquid Crystal Materials Research Center, University of Colorado Boulder, Boulder, CO 80309; [c]Max-Planck-Institut für Intelligente Systeme, D-70569 Stuttgart, Germany; [d]IV Institut für Theoretische Physik, Universität Stuttgart, D-70569 Stuttgart, Germany; [e]Department of Electrical, Computer, and Energy Engineering and Materials Science and Engineering Program, University of Colorado Boulder, Boulder, CO 80309; and [f]Renewable and Sustainable Energy Institute, National Renewable Energy Laboratory and University of Colorado Boulder, Boulder, CO 80309

Edited by John D. Weeks, University of Maryland, College Park, MD, and approved March 5, 2015 (received for review January 20, 2015)

Geometric shape and topology of constituent particles can alter many colloidal properties such as Brownian motion, self-assembly, and phase behavior. Thus far, only single-component building blocks of colloids with connected surfaces have been studied, although topological colloids, with constituent particles shaped as freestanding knots and handlebodies of different genus, have been recently introduced. Here we develop a topological class of colloids shaped as multicomponent links. Using two-photon photopolymerization, we fabricate colloidal microparticle analogs of the classic examples of links studied in the field of topology, the Hopf and Solomon links, which we disperse in nematic fluids that possess orientational ordering of anisotropic rod-like molecules. The surfaces of these particles are treated to impose tangential or perpendicular boundary conditions for the alignment of liquid crystal molecules, so that they generate a host of topologically nontrivial field and defect structures in the dispersing nematic medium, resulting in an elastic coupling between the linked constituents. The interplay between the topologies of surfaces of linked colloids and the molecular alignment field of the nematic host reveals that linking of particle rings with perpendicular boundary conditions is commonly accompanied by linking of closed singular defect loops, laying the foundations for fabricating complex composite materials with interlinking-based structural organization.

liquid crystals | self-assembly | topological defects | Hopf and Solomon links | low-dimensional topology

Interlocking closed loops in physical field lines (1–3), small molecules (4), DNA and synthetic polymer chains (5), and various vortices (6–8) can lead to new physical behavior, biological functionality, and material properties that largely stem from the underlying topology (1). For example, linking looped lines of the liquid crystal (LC) molecular alignment field $\mathbf{n}(\mathbf{r})$ (3), which describes spatial changes in local average orientations of constituent rod-like molecules (9), causes formation of topologically protected particle-like structures resembling mathematical Hopf and Seifert fibrations (1, 3, 10, 11). Similar field configurations with linked closed loops or linked torus knots of field lines are also predicted to exist in electromagnetic fields (2, 12, 13), in Bose-Einstein condensates (14, 15), and in magnetization of various ferromagnets (16–18), often defining novel types of physical behavior that arise from topological stabilization of such field configurations. However, the implications of topological linking on behavior of colloidal particles have not been considered thus far, neither experimentally nor theoretically, although many types of complex-shaped colloidal particles have been recently fabricated (8, 19, 20).

In this work, we fabricate micrometer-sized colloidal particles with differently linked components shaped as closed solid polymeric rings with disconnected surfaces that, when dispersed in a fluid host like water or LC, undergo Brownian motion both relative to each other and as a whole. In a nematic LC host (8, 19–23), these particles induce a large variety of field configurations and looped and linked vortex lines that entangle the linked components of the colloidal particles, resulting in elastic coupling between them. Using a combination of 3D nonlinear optical imaging, videomicroscopy, and noncontact laser manipulation (8, 24, 25), we characterize the interplay between topologies of colloidal surfaces, $\mathbf{n}(\mathbf{r})$ configurations, and defects, as well as probe the strength of elastic coupling between the colloidal particle's components. We supplement these experiments with a theoretical analysis based on numerical minimization of the bulk Landau-de Gennes and surface anchoring free energies (26–29) that yields configurations topologically homeomorphic to experimental counterparts. Finally, we discuss the prospects for interlocking-based assembly of composite materials and for experiment-driven fundamental explorations of topological interaction of physical links with nonpolar fields.

Results and Discussion

Using two-photon photopolymerization, we realize colloidal building blocks with topology of the classical Hopf link (Fig. 1 *A* and *B*), consisting of two colloidal rings linked together once, the simplest two-component link (1). They are characterized by a numerical invariant $Lk = \pm 1$, dubbed "linking number" (1), representing the number of times that each closed colloidal loop winds around the other, with the sign dependent on the choice of orientations of the linked components (1). In the colloidal Solomon's link of $Lk = \pm 2$ (Fig. 1 *C* and *D*), two closed, photopolymerized rings are doubly interlinked in an alternating manner, so that this colloidal building block exhibits four crossings of the two loops interweaving under and over each other (1). 3D nonlinear optical imaging (Fig. 1 *B* and *D*) reveals that surfaces of the two linked components stay separated from each other, consistent with the topology of Hopf and Solomon links.

When introduced into a nematic host (Fig. 2), as-fabricated linked particles define tangential boundary conditions for $\mathbf{n}(\mathbf{r})$ at

Significance

Colloidal dispersions are abundant in nature, fundamental science, and technology, with examples ranging from fog and milk to colloidal models of atomic crystals and glasses and colloidal quantum dots used in fabricating the third-generation solar cells. Despite the recent progress in exquisite control of geometric shape and topology of constituent colloidal particles, thus far only single-component colloidal building blocks have been fabricated or found occurring in nature. We develop multicomponent linked colloidal particles lacking connectivity of their surfaces, with each component behaving as a genus-one colloidal particle itself but being topologically linked with the other components within a colloidal building block. We uncover topological property-defining behavior of such colloidal particles when dispersed in a nematic liquid crystal medium.

Author contributions: I.I.S. designed research; A.M., L.H., M.T., and I.I.S. performed research; I.I.S. contributed new reagents/analytic tools; A.M., M.T., and I.I.S. analyzed data; and A.M. and I.I.S. wrote the paper.

The authors declare no conflict of interest.

This article is a PNAS Direct Submission.

[1]To whom correspondence should be addressed. Email: ivan.smalyukh@colorado.edu.

This article contains supporting information online at www.pnas.org/lookup/suppl/doi:10.1073/pnas.1500998112/-/DCSupplemental.

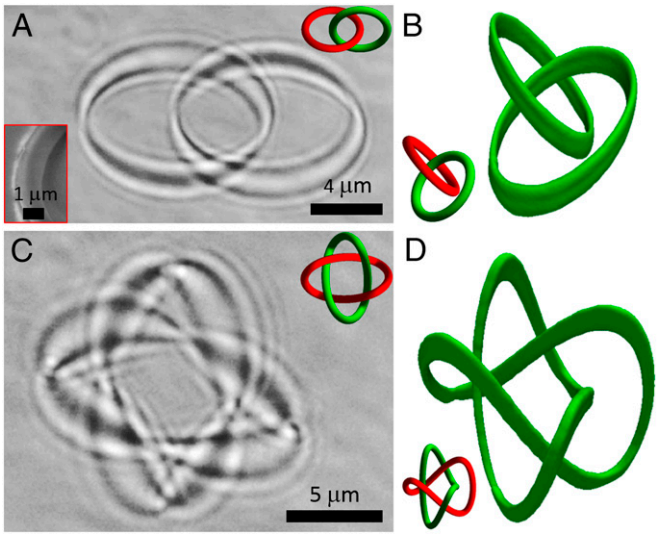

Fig. 1. Photopolymerized colloidal links. (*A*) An optical brightfield micrograph of a Hopf link particle and (*Upper Right Inset*) the corresponding 3D model. (*Lower Left Inset*) Scanning electron microscopy image of a photopolymerized tube from which all linked particles are made. (*B*) A 3D perspective view of the same Hopf link particle (corresponding to the model shown in the *Inset*) obtained using 3PEF-PM; the high-intensity fluorescence signal from the particle is shown in green. (*C*) An optical brightfield micrograph of a Solomon link particle and (*Inset*) the corresponding 3D model. (*D*) A 3D perspective view of the same Solomon link (corresponding to the model shown in the inset) obtained using 3PEF-PM.

their surfaces. Of several observed $\mathbf{n}(\mathbf{r})$ configurations induced by Hopf link colloids (Figs. 2 and 3 and *SI Appendix*, Fig. S1), the most common one contains eight surface point defects, dubbed "boojums," with four on each of the linked colloidal rings having their planes tilted away from the far-field director $\mathbf{n}_0$ by 10–30°, depending on the particle (Fig. 2). Elastic distortions weakly couple the two linked components, defining the equilibrium center-to-center distance and locations at which the linked rings cross the planes of each other (Fig. 2*E*, *Inset*), as well as the equilibrium angle between the center-to-center separation vector and $\mathbf{n}_0$. These elastic forces also stabilize the linked components against touching each other. Using videomicroscopy, we probe changes of the center-to-center distance, d-d_{avg}, and the angle that the separation vector makes with $\mathbf{n}_0$, α-α_{avg}, away from their equilibrium values d_{avg} and α_{avg}, respectively, under the influence of thermal fluctuations (Fig. 2*E*). In both cases, the behavior is Hookean-like and can be characterized by spring constants k_d = 1.51 pN/μm and k_α = 24.45 pN·μm, respectively. Metastable colloidal and field configurations with different orientations of rings and different numbers of boojums are also observed, including those without boojums (Fig. 2 *I* and *J*) and with one boojum-free ring perpendicular to $\mathbf{n}_0$ linked to a ring with four boojums (Fig. 3*F* and *SI Appendix*, Fig. S1 *E* and *F*). These configurations also exhibit elastic coupling between the linked rings and with the orientation of $\mathbf{n}_0$. The boojums have split-core structure (Fig. 2*F*, *Lower Right Inset*) in the form of semiloops of half-integer defect lines, similar to other colloids with tangential anchoring (28, 29), and appear in self-compensating pairs of opposite winding numbers, consistent with the zero Euler characteristic of the individual rings of our multicomponent particles.

Even more exotic behavior of linked nematic colloids is observed when their surfaces are treated to impose homeotropic (perpendicular) boundary conditions for $\mathbf{n}(\mathbf{r})$ (Figs. 4–6 and *SI Appendix*, Fig. S2). These particles tend to induce singular defect lines, which can be associated with individual colloidal components (Fig. 5) or jump from the proximity of one component to the other (Figs. 4 and 6 and *SI Appendix*, Fig. S2). In addition to the purely elastic coupling, the colloidal components become entangled by unknots of defect lines (22, 30) that act as elastic strings. The Hookean-like behavior describing angular and translational deviations of relative positions of rings and orientation of their center-to-center separation vector away from equilibrium for the particle shown in Fig. 5 are characterized by

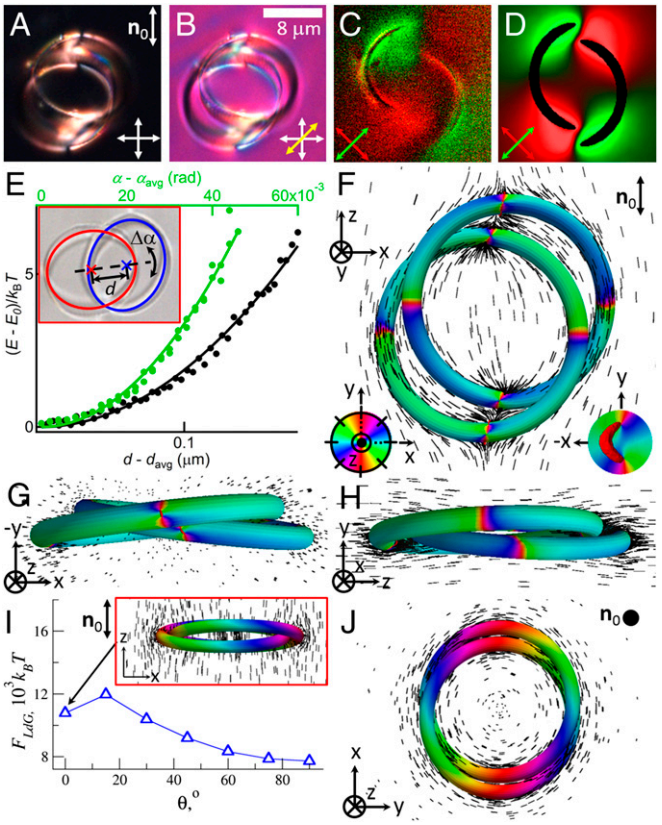

Fig. 2. A Hopf link colloidal particle with tangential anchoring in an aligned nematic LC. (*A* and *B*) Polarizing optical micrographs of a colloidal Hopf link in a nematic cell with $\mathbf{n}_0$ marked on the image as viewed between (*A*) crossed polarizers (white double arrows) and (*B*) between crossed polarizers and an additional 530-nm wave plate (yellow double arrow) with a slow axis at 45° to them. (*C*) An in-plane cross-sectional composite 3PEF-PM image of a Hopf link and $\mathbf{n}(\mathbf{r})$ around it obtained by superimposing two 3PEF-PM scans (with fluorescence shown in green and red colors) acquired using orthogonal, linear polarizations of excitation light along directions depicted by green and red double arrows. (*D*) The corresponding theoretical 3PEF-PM cross section based on the numerically calculated $\mathbf{n}(\mathbf{r})$ shown in *F–H*; the green and red colors in the composite texture correspond to 3PEF-PM signals at polarizations of excitation light along the green and red double arrows marked on the image. (*E*) Elastic interaction energy vs. deviation from the equilibrium center-to-center separation d-d_{avg} (d_{avg} = 6.99 μm, black symbols and scale) and deviation from the equilibrium orientation α-α_{avg} (α_{avg} = 1.52 rad, green symbols and scale). (*Inset*) Center-to-center distance and orientation, which were studied using videomicroscopy. (*F–H*) Three perspective views from mutually orthogonal directions of a numerically calculated $\mathbf{n}(\mathbf{r})$ depicted using colors on the particle's surfaces and using rods in the LC bulk nearby. The colors on the particle surfaces show azimuthal orientations of $\mathbf{n}(\mathbf{r})$ with respect to $\mathbf{n}_0$ according to the color scheme shown in the *Lower Left Inset* of *F*. (*Lower Right Inset*) Details of the core structure of a boojum splitting into a semiloop of a half-integer defect line with the handle-shaped region of reduced order parameter shown in red. (*I*) Landau-de Gennes free energy vs. angle θ between $\mathbf{n}_0$ and the plane bisecting the angle θ_{12} = 20° between the rings at fixed radius R and d = 0.22R, with the energy minimum corresponding to the configuration (*F*). *Inset* of *I* and panel *J* show two perspective views of a metastable configuration of the particle and $\mathbf{n}(\mathbf{r})$ without boojums from mutually orthogonal directions.

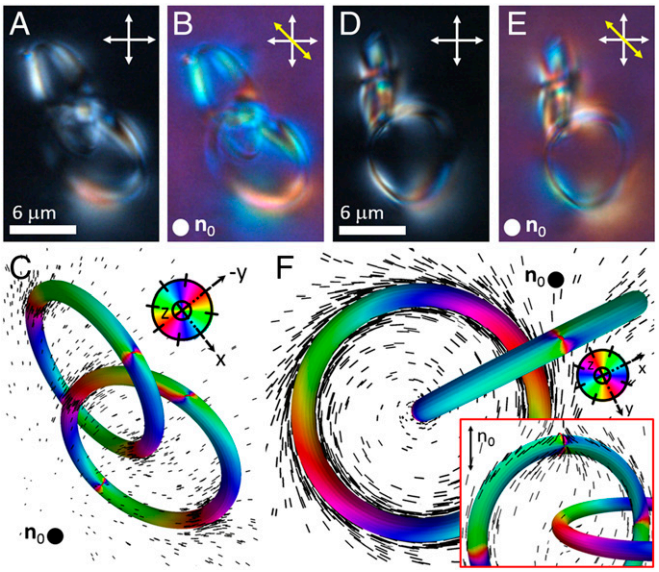

Fig. 3. Metastable configurations of colloidal Hopf links with tangential surface anchoring in an aligned LC. (*A, B, D,* and *E*) Polarizing optical micrographs of Hopf link particles in a homeotropic nematic cell viewed between (*A* and *D*) crossed polarizers marked by white double arrows and (*B* and *E*) between crossed polarizers and an additional inserted 530-nm wave plate with a slow axis at 45° to them (yellow double arrow). (*C* and *F*) The corresponding numerically calculated $\mathbf{n}(\mathbf{r})$ is depicted using colors on the particles' surfaces and using rods in the LC bulk nearby; *Inset* in *F* shows a different perspective view of the corresponding colloidal link. The colors on the particles surfaces show azimuthal orientations of $\mathbf{n}(\mathbf{r})$ with respect to $\mathbf{n}_0$ according to the color schemes shown in *Insets*. The theoretical configurations shown in *C* and *F* resemble those depicted in *A* and *B* and *D* and *E*, respectively; note that one of the rings in *F* contains no boojums.

spring constants $k_d = 1.4$ pN/μm and $k_\alpha = 176.9$ pN·μm, respectively. Despite the constraints on the overall zero bulk hedgehog charges of defects imposed by topological theorems (19), the nonpolar nature of $\mathbf{n}(\mathbf{r})$, combined with the rich configuration space of the colloid itself, permits to accommodate topologically distinct configurations of closed defect loops, including the ones in which they are linked with none, one, or both colloidal ring components, or with other defect loops (Figs. 4 and 5 and *SI Appendix*, Fig. S2), or unlinked ones (Fig. 6). Importantly, the individual linked components of a colloidal entity move with respect to each other while having field configurations governed by the elasticity of the surrounding nematic fluid. They are thus elastically kept at separations and orientations (Fig. 5*E*) corresponding to local or global minima of free energy associated with the metastable or equilibrium states, respectively.

As the particle's linking number increases, so does the complexity of the observed field and defect configurations (Figs. 7 and 8 and *SI Appendix*, Figs. S3 and S4). Colloidal Solomon links with tangential boundary conditions (26–29) tend to induce, on average, two times more boojums than their Hopf counterparts, with these surface point defects commonly seen at the regions of highest curvature at the tip points of the tubes forming the linked colloidal rings (Fig. 7). The large number of stable and metastable mutual positions and orientations of the linked components, as well as their orientation with respect to $\mathbf{n}_0$, lead to diverse field configurations differing by the number of generated boojum-antiboojum pairs characterized by self-compensating, opposite winding numbers (Fig. 7 *C* and *F*) (26). The most frequently observed configuration due to a Solomon link with perpendicular surface boundary conditions involves pairs of individual looped defect lines following each of the linked components (Fig. 8 *D* and *E*), locally resembling defects induced by trefoil knots (8).

Experimental and theoretical particle-induced $\mathbf{n}(\mathbf{r})$ structures are mutually consistent, although some metastable structures are observed only in experiments (*SI Appendix*, Figs. S2–S4) or only in theory (*SI Appendix*, Figs. S1 and S5–S10). All field and defect configurations induced by linked colloids with tangential anchoring and of a given Lk can be obtained from each other through smooth deformation of $\mathbf{n}(\mathbf{r})$, rotations and translations of linked components, and annihilation or generation of pairs of boojums with opposite winding numbers. Because the studied particles have linked constituents of Euler characteristic $\chi = 0$, there is always an equal number of boojums with opposite winding numbers and with bulk hedgehog topological charges adding to zero. Particles of the same linking number Lk and perpendicular boundary conditions can induce configurations of defect loops, which cannot be continuously transformed from one to another. For example, in the case of Hopf link colloids we observe two to four closed loops of half-integer defect lines, which can be linked with a single or both colloidal rings or with each other. Topologically distinct configurations induced by Hopf link colloids and the corresponding graphs are summarized in Fig. 9. The graphs show that the number of linking connected, inseparable graph entities can range from one, when all particle and defect rings are interlinked, to five, when Hopf link particles are accompanied by four unlinked defect loops (Fig. 9). These mixed, defect-colloidal, multicomponent links cannot be morphed from one to another, unless crossing, splitting, or merging of defect loops are allowed to occur. The associated energetic barriers thus stabilize the distinct topologies of the defect-colloidal multicomponent links that we can distinguish based on the total number of unknots in forms of colloidal rings or defect loops and the number of links between them visible from simplified topological skeletons and graph representations (*Inset* of Fig. 8*D* and Fig. 9). The states summarized in Fig. 9, with simplified presentations of topology that correspond to local and global minima of free energy, do not exhaust all topology-admissible structural varieties of field configurations, but it is interesting that a single Hopf link of colloidal rings can be accompanied by up to four defect loops with up to 9 links between them (*SI Appendix*, Fig. S10) while in long-lived metastable states, allowing for a detailed experimental exploration of the interplay between topologies of particles, fields, and defects. The complexity increases further as one considers

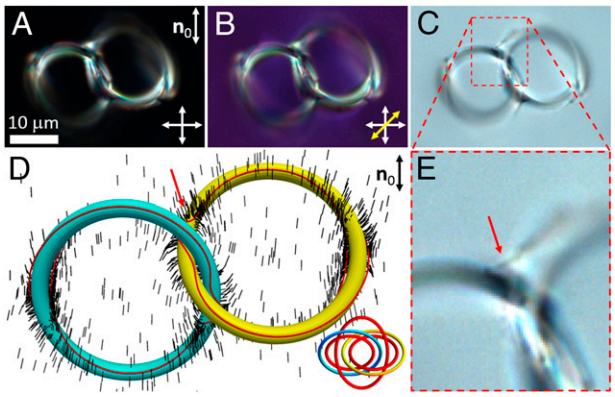

Fig. 4. A colloidal Hopf link with perpendicular surface boundary conditions in an aligned nematic LC. (*A* and *B*) Optical micrographs of a Hopf link particle in a nematic LC with $\mathbf{n}_0$ marked on the image viewed between (*A*) crossed polarizers (white double arrows), (*B*) between crossed polarizers and an additional inserted 530-nm wave plate with a slow axis at 45° to them (yellow double arrow), and (*C*) without polarizers or wave plate. (*D*) A theoretical model of the studied colloidal Hopf link configuration, with $\mathbf{n}(\mathbf{r})$ shown by rods and defect lines as red lines. (*Inset*) Topological skeleton of linked colloidal and defect loops. (*E*) A zoom-in view of *C* focusing on the jumping disclination seen in both experiments and theoretical modeling, which we mark by red arrows in *D* and *E*.

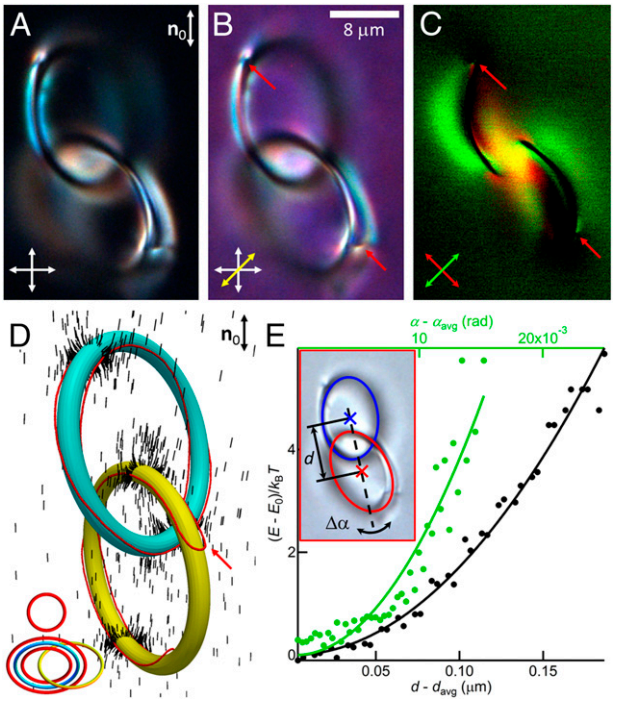

Fig. 5. A metastable configuration of a colloidal Hopf link with perpendicular boundary conditions in a nematic cell. (*A* and *B*) Optical micrographs of a Hopf link particle in a nematic LC with $\mathbf{n}_0$ marked on the image viewed between (*A*) crossed polarizers (white double arrows) and (*B*) between crossed polarizers and an additional inserted 530-nm wave plate with a slow axis at 45° to them (yellow double arrow). (*C*) An in-plane cross-sectional composite 3PEF-PM image of a Hopf link and $\mathbf{n}(\mathbf{r})$ around it obtained by superimposing two 3PEF-PM scans (green and red colors) acquired using orthogonal, linear polarizations of excitation light along directions depicted by green and red double arrows. (*D*) A 3D theoretical model of the colloidal Hopf link $\mathbf{n}(\mathbf{r})$-configuration (shown by rods) and defect lines (red closed loops). Locations of defect lines are marked by red arrows in *B*–*D*. (*Inset*) Topological skeleton of linked colloidal and defect loops. (*E*) Elastic interaction energy vs. deviation from the equilibrium center-to-center separation d-d_{avg} (d_{avg} = 10.93 μm, black symbols and scale) and deviation from the equilibrium orientation $\Delta\alpha$=α-α_{avg} (α_{avg} = 0.19 rad, green symbols and scale) defined in *Inset*.

higher-order links of knotted loops of solid colloidal particles in LCs, so we present only the simplest examples of observed colloidal and director structures due to Solomon links (Fig. 8 and *SI Appendix*, Fig. S4).

Inseparability of the linked particle components considerably enriches their physical behavior. Unlike in conventional colloids, many-body interactions can exist among the linked components belonging to the same composite particle, constrained by the physical linking, or to different multicomponent particles. LC elasticity-mediated interactions between the linked rings of the same particle and the surrounding LC matrix are different from what one would expect for two unlinked rings with similar induced defects. For example, unlinking of the rings shown in Fig. 2, with four induced boojums per each ring, is expected to result in quadrupolar interactions and self-assembly similar to what we studied previously (19, 20), very different from the equilibrium and metastable mutual arrangements of component rings of the linked pair (Figs. 2 and 3). Unlike the unlinked colloidal rings with perpendicular boundary conditions, which can exhibit both ring-like and point defects (19), their linked counterparts have not been observed to induce point singularities. Unlinked loops of half-integer defect lines (Fig. 9) can be topologically equivalent to point defects of hedgehog charge ±1, and additional self-compensating ±1 point defect pairs can be always introduced without violating topological charge conservation (19). However, the free energy minimization of elastic distortions induced by complex-shaped particles with the topology of links yields free energy minima for field configurations with linear defect loops (some of which are linked with each other and with the particles). Sharing or linking of defect loops induced by the linked rings provides an additional interaction mechanism due to the defect line tension (Fig. 4), which is of the order of 50–70 pN for singular half-integer defect lines (26, 30). Defect-entangled colloidal configurations, like the one shown in Fig. 4, can have the colloidal component rings touching each other or (most commonly) not, depending on the competition of the defect line tension and repulsive elastic forces due to strong director distortions when two such rings approach each other. When the component rings touch, the colloid undergoes Brownian motion as an effective genus $g = 2$ handlebody, with surface topology distinct from that of two separate rings. Beyond LC colloids, linking can alter interactions between colloidal components when, for example, interactions originate from electrostatic or depletion forces, opening a new avenue for designing complex colloidal self-assembly architectures and functionality. On the other hand, our system with elastic closed loops of defect lines may provide an experimental platform for testing predictions of mathematical models for minimum ropelength of linked and knotted topological configurations (31), as well as a basis for expanding such models to more complex cases of linked and knotted loops elastically repelling from each other, as in some of our experiments.

To conclude, we developed a class of topological colloidal particles with multiple linked components. We demonstrated that, when dispersed in nematic fluids, linked colloidal building blocks induce field-defect configurations that can be topologically distinct from each other, but always satisfy the topological constraints. Although we considered only uniform tangential and perpendicular boundary conditions on all surfaces of colloidal building blocks, this study can be extended to patched, mixed, and optically controlled boundary conditions (32), potentially allowing for dynamic reconfigurability. In addition to linked genus-one rings, one can envision complex but interesting behavior of linked particles with a larger genus (19) and a larger number of linked components. For example, a defect line emanating from the surface of one linked large-genus colloidal component with tangential boundary conditions could

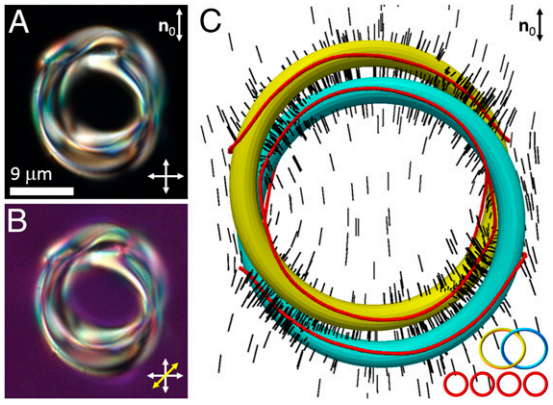

Fig. 6. A compact metastable configuration of a colloidal Hopf link with perpendicular surface boundary conditions in a nematic LC. (*A* and *B*) Optical micrographs of a metastable-state Hopf link particle in a nematic LC with $\mathbf{n}_0$ marked on the image as viewed between (*A*) crossed polarizers (white double arrows) and (*B*) between crossed polarizers and an additional inserted 530-nm wave plate with a slow axis at 45° to them (yellow double arrow). (*C*) A 3D theoretical model of the studied colloidal Hopf link $\mathbf{n}(\mathbf{r})$ configuration (shown by rods) and defect lines (red closed loops), with its simplified topological skeleton shown in *Inset*.

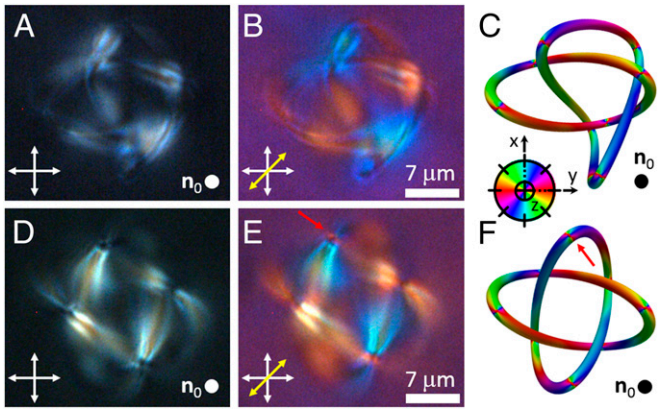

Fig. 7. Colloidal Solomon links with tangential surface boundary conditions in a nematic LC. (*A* and *B*) A Solomon link in a homeotropically aligned nematic cell as viewed between (*A*) crossed polarizers aligned along the white arrows and (*B*) between crossed polarizers and an additional 530-nm wave plate with slow axis at 45° to them (yellow double arrow). (*C*) A numerical model of **n**(**r**) depicted using colors on the particle surfaces corresponding to the experimental images shown in *A* and *B*. The colors on the particle surfaces show azimuthal orientations of **n**(**r**) with respect to $\mathbf{n}_0$ (normal to the page) according to the color scheme shown in *Inset*. (*D* and *E*) Another configuration for a tangentially anchored Solomon link in a homeotropic nematic cell viewed between (*D*) crossed polarizers without and (*E*) with an inserted additional wave plate. (*F*) Numerically calculated **n**(**r**) depicted using colors on the particle surfaces corresponding to the experimental images shown in *D* and *E*.

terminate on another one, binding both components. In this way, valence-like interactions (33) between the components of the colloidal building blocks could emerge. Experimental study of implications of linking of particles and defect loops in terms of the topology-dictated appearance of additional defects could also allow for new means of probing symmetry of LC phases, e.g., distinguishing between uniaxial and biaxial nematics (34), as well as expand the diversity of soft matter systems generating topologically nontrivial configurations (3, 7, 8, 19, 35–37). Other needed future explorations include stability analysis and study of structural phase diagrams, as well as how cell confinement, kinetic processes, chirality, surface nonorientability of linked colloidal components, and external fields control them (35–37). Linked multicomponent particles dispersed in LC or isotropic hosts, with the components made of the same or different materials, are of practical interest as they can enrich colloidal self-assembly and response to external stimuli.

Materials and Methods

Sample Preparation. We used LC cells constructed from two glass substrates, coated either with a thin film of rubbed polyimide (PI-2555; HD Microsystems) or a monolayer of *N*,*N*-dimethyl-*N*-octadecyl-3-aminopropyltrimethoxysilyl chloride (DMOAP) to induce planar or perpendicular boundary conditions at the LC-substrate interfaces, respectively. We spaced the substrates with 25- to 30-μm silica spheres mixed into UV-curable glue (NOA-65; Norland), setting the cell gap thickness. Once cured, we sealed two sides of the cell with epoxy and then used capillary action to fill it with a dispersion of linked particles in a single-compound nematic LC pentylcyanobiphenyl (5CB, used to obtain data shown in Figs. 2, 4, 5, 6, and 8 and *SI Appendix*, Figs. S2, S4, S12, and S13) or in a mixture ZLI-2806 (used to obtain Figs. 3 and 7 and *SI Appendix*, Fig. S3), both purchased from EM Chemicals. For 3PEF-PM imaging, colloidal dispersions based on ZLI-2806 were doped with ∼1 Wt.% of 5CB. For planar cells with rubbed polyimide, the LC flow during filling was chosen to be along the rubbing direction. Once the cell was filled, we sealed the two remaining edges with epoxy. Finally, the LC was heated to isotropic phase and quenched back to nematic phase to mitigate flow-induced alignment effects.

Fabrication of Particles and Their Dispersion in LCs. The linked colloidal building blocks (Fig. 1) were fabricated using a two-photon polymerization system shown in *SI Appendix*, Fig. S11 (8). The setup was constructed around a home-built inverted microscope with a computer-guided 3D nano-positioning stage (model P-611.3SF, 0.2-nm resolution; Physik Instrumente). A laser beam from a femtosecond Ti:sapphire oscillator (from Coherent) at 780 nm wavelength first passes through a half-wave plate and a Glan polarizer (for power control) and then through two lenses, forming a telescope designed to expand its diameter from the initial 3 mm to about 5 mm to properly fill the back aperture of an objective lens. At the location between two telescope lenses where their foci meet (*SI Appendix*, Fig. S11), we placed a 100-μm pinhole, which improves the beam quality through spatial filtering, and a computer-controlled fast shutter (model LS3Z2, 200 Hz; Uniblitz). After the telescope, the beam was directed into the back aperture of the objective by mirrors, with the last dichroic mirror right before the objective reflecting light of wavelengths >750 nm and transmitting visible light. This spectral separation allowed us to monitor the polymerization process in real time using brightfield microscopy and a charge-coupled device camera. Guided by our LabView-based software, the fast shutter and the nano-stage operated in concert. The shutter opened at the beginning and closed at the end of each particle-defining 3D trajectory. The spatial translation of the 3D nano-stage with a sample mounted on it was done in such a way that a focused femtosecond beam followed a trajectory prescribed by a set of parametric equations (*SI Appendix*), yielding polymerized particles of desired topology (Movies S1 and S2). The cross-sectional tube diameter of each closed ring in the multicomponent colloidal links was tuned from 0.3 to 3 μm, and the overall size of particles was varied from 3 to 20 μm. The average laser power used for polymerization ranged from 3 mW for small particles to 13 mW for the larger ones. Linked particles were photopolymerizied within a specially constructed cell (*SI Appendix*, Fig. S11) suspending a droplet of IP-L 780 photoresist (NanoScribe GmbH), which cross-links (solidifies) when exposed to the high-intensity femtosecond laser light at 780 nm. This polymerization was done within glass cells consisting of a standard microscope slide and

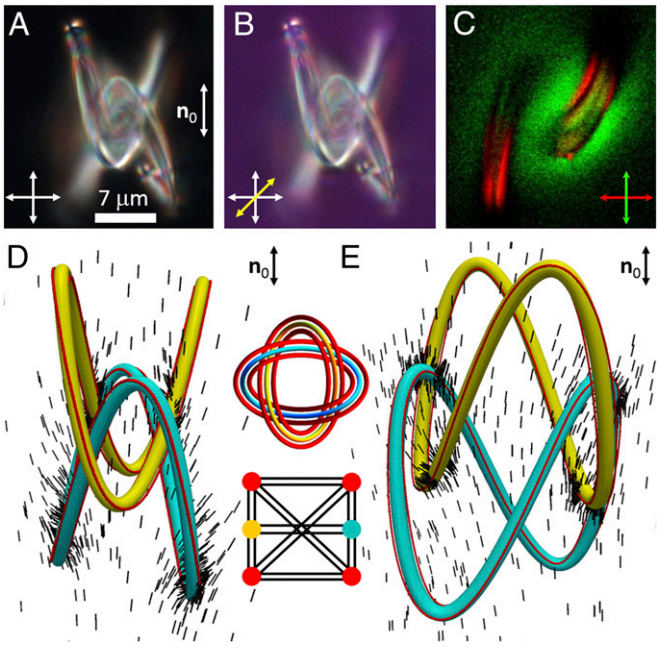

Fig. 8. A Solomon link particle with homeotropic surface boundary conditions in a nematic LC. (*A* and *B*) Optical micrographs of the particle as viewed between (*A*) crossed polarizers (white double arrows) without and (*B*) with an inserted 530-nm wave plate with a slow axis at 45° to them (yellow double arrow). (*C*) An in-plane cross-sectional composite 3PEF-PM image of a Solomon link and **n**(**r**) around it obtained by superimposing two scans acquired using orthogonal, linear polarizations of excitation light along directions depicted by green and red double arrows; fluorescence signals of the composite image corresponding to the two polarizations of excitation light are shown in green and red colors, respectively. (*D* and *E*) Two perspective views of a 3D theoretical model of the studied colloidal Solomon link revealing **n**(**r**) (shown by rods) and defect lines (red closed loops). In *Insets* in *D*, the mutually linked, physical-particle unknots are shown as blue and yellow rings and filled circles, and the defect line loops are shown as red loops and filled circles, respectively; double links are indicated by double black edges connecting the corresponding red-blue-yellow filled circles that represent defect or colloidal rings.

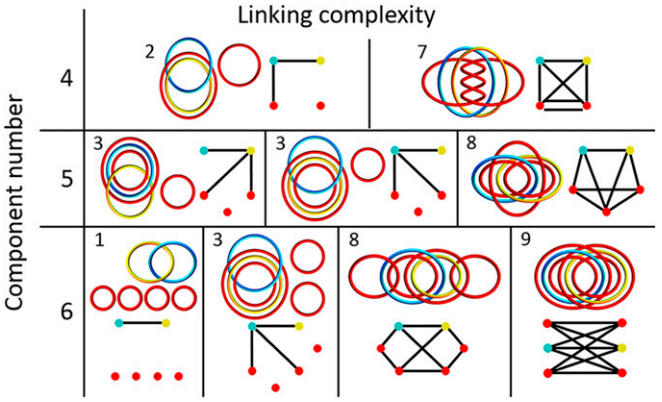

Fig. 9. Topological skeletons and graphical representations of interlinked Hopf link particles and accompanying closed defect loops. The mutually linked, physical-particle rings are shown in blue and yellow colors, and the defect line loops are shown in red. In the graphs, the individual links are indicated by black edges connecting the corresponding red-blue-yellow filled circles that represent colloidal or defect rings; the overall number of links is indicated next to the topological skeleton representations of structures reconstructed from data (Figs. 4–6 and *SI Appendix*, Figs. S2 and S5–S10).

a 170-μm-thick coverslip, spaced by 50-μm-thick Mylar strips. As the beam focus was translated through the monomeric fluid, we always began polymerization at the substrate-fluid interface to effectively anchor the structure while it is being drawn. Arrays of particles were then detached from substrates by gentle sonication and dispersed into LCs. As-manufactured particles impose tangential boundary conditions for **n**(**r**), but some of them were treated with DMOAP for perpendicular ones (8).

Optical Imaging and Laser Manipulation. Director structures are studied using a combination of conventional polarizing optical microscopy and a 3D nonlinear imaging technique dubbed "three-photon excitation fluorescence polarizing microscopy" (3PEF-PM) (25), which is based on fluorescence of LC molecules excited through three-photon absorption of femtosecond infrared laser light. The 3PEF-PM fluorescence intensity exhibits a strong well-defined dependence (25) on the orientation of linear polarization of the excitation beam relative to **n**(**r**). 3PEF-PM images, comprised of 3D stacks of optical slices, such as the ones shown in the SI Appendix, Figs. S12 and S13 and Movies S3–S5, reveal orientations and relative positions of linked rings as well as the corresponding locations and configurations of topological defects accompanying them. Close analysis of 3PEF-PM stacks reveals dependence of 3D **n**(**r**)-structures on boundary conditions and topology of colloids. Optical videomicroscopy and holographic laser tweezers (25) probe elastic interactions between the linked rings. Additionally, high-power beams of laser tweezers allow for locally melting the LC around particles and then quenching it back to the nematic phase, thus probing different stable and metastable configurations.

Theoretical Modeling of Field and Defect Structures. Director configurations around colloidal particles were obtained via numerical minimization of the phenomenological Landau-de Gennes free energy functional (26) supplemented by a surface anchoring free energy term (9, 27–29) to account for finite-strength boundary conditions on particle surfaces. The surfaces of linked particles in a nematic bulk are defined for interring separation and mutual orientation of the linked colloidal components with respect to $\mathbf{n}_0$ determined from experiments. The total free energy is then minimized using the adaptive finite-element method (28) and experimental material and geometric parameters, as described in details in *SI Appendix*, Table S1 and Figs. S14–S18.

Direct Comparison of Theory and Experiments. 3D 3PEF-PM images are simulated based on known dependencies (25) of the fluorescence signal from LC on the polarization of excitation light while accounting for the finite resolution effects and the changes of this polarization state as it is traversing the LC medium using the Jones matrix method and numerically simulated **n**(**r**), as described in *SI Appendix*. Fig. 2 *C* and *D* provides an example of a direct comparison of a single slice out of a 3D experimental 3PEF-PM image with its theoretical counterpart.

ACKNOWLEDGMENTS. We acknowledge discussions with P. J. Ackerman, M. Bowick, N. Clark, R. Kusner, T. C. Lubensky, D. Phillips, and B. Senyuk. This work was supported by a National Science Foundation Grant DMR-0820579 (to A.M. and I.I.S.), American Chemical Society Petroleum Research Fund Grant PRF 54095-ND7 (to I.I.S.), and partially by the 7th Framework Programme International Research Staff Exchange Scheme Marie-Curie Grant PIRSES-GA-2010-269181 (to M.T.).

1. Kauffman LH (2000) *Knots and Physics* (World Scientific Publishing, Singapore).
2. Irvine WTM, Bouwmeester D (2008) Linked and knotted beams of light. *Nat Phys* 4(9):716–720.
3. Smalyukh II, Lansac Y, Clark N, Trivedi R (2010) Three-dimensional structure and multistable optical switching of triple-twisted particle-like excitations in anisotropic fluids. *Nat Mater* 9(2):139–145.
4. Pentecost CD, et al. (2007) A molecular solomon link. *Angew Chem Int Ed Engl* 46(1-2): 218–222.
5. Hadjichristidis N, Hirao A, Tezuka Y, Du Prez F, eds (2011) *Complex Macromolecular Architectures* (Wiley, Singapore).
6. Kleckner DM, Irvine WTM (2013) Creation and dynamics of knotted vortices. *Nat Phys* 9(4):253–258.
7. Tkalec U, Ravnik M, Čopar S, Žumer S, Muševič I (2011) Reconfigurable knots and links in chiral nematic colloids. *Science* 333(6038):62–65.
8. Martinez A, et al. (2014) Mutually tangled colloidal knots and induced defect loops in nematic fields. *Nat Mater* 13(3):258–263.
9. Chaikin PM, Lubensky TC (1995) *Principles of Condensed Matter Physics* (Cambridge Univ Press, Cambridge, UK).
10. Hopf H (1931) Über die Abbildungen der dreidimensionalen Sphäre auf die Kugelfläche. *Mathematische Annalen* 34:637–665.
11. Whitehead JHC (1947) An expression of Hopf's invariant as an integral. *Proc Natl Acad Sci USA* 33(5):117–123.
12. Ronada AF, Trueba JL (1996) Ball lightning an electromagnetic knot? *Nature* 383(6595):32.
13. Ronada AF, Trueba JL (1995) Electromagnetic knots. *Phys Lett A* 202:337–342.
14. Kawaguchi Y, Nitta M, Ueda M (2008) Knots in a spinor Bose-Einstein condensate. *Phys Rev Lett* 100(18):180403.
15. Liu Y-K, Zhang C, Yang S-J (2013) 3D skyrmion and knot in two-component Bose–Einstein condensates. *Phys Lett A* 377(45-48):3300–3303.
16. Cooper NR (1999) 'Smoke rings' in ferromagnets. *Phys Rev Lett* 82:1554–1557.
17. Sutcliffe P (2007) Vortex rings in ferromagnets. *Phys Rev B* 76:184439.
18. Borisov AB, Rybakov FN (2009) Dynamical toroidal Hopfions in a ferromagnet with easy axis anisotropy. *JETP Lett* 90:544–547.
19. Senyuk B, et al. (2013) Topological colloids. *Nature* 493(7431):200–205.
20. Lapointe CP, Mason TG, Smalyukh II (2009) Shape-controlled colloidal interactions in nematic liquid crystals. *Science* 326(5956):1083–1086.
21. Poulin P, Stark H, Lubensky TC, Weitz DA (1997) Novel colloidal interactions in anisotropic fluids. *Science* 275(5307):1770–1773.
22. Lubensky TC, Pettey D, Currier N, Stark H (1998) Topological defects and interactions in nematic emulsions. *Phys Rev E Stat Nonlin Soft Matter Phys* 57(1):610–625.
23. Alexander GP, Chen BG, Matsumoto EA, Kamien RD (2012) Colloquium: Disclination loops, point defects, and all that in nematic liquid crystals. *Rev Mod Phys* 84:497–514.
24. Trivedi RP, Engström D, Smalyukh II (2011) Optical manipulation of colloids and defect structures in anisotropic liquid crystal fluids. *J Opt* 13:044001.
25. Trivedi RP, Lee T, Bertness KA, Smalyukh II (2010) Three dimensional optical manipulation and structural imaging of soft materials by use of laser tweezers and multimodal nonlinear microscopy. *Opt Express* 18(26):27658–27669.
26. de Gennes PG, Prost J (1993) *The Physics of Liquid Crystals* (Clarendon, Oxford), 2nd Ed.
27. Fournier JB, Galatola P (2005) Modeling planar degenerate wetting and anchoring in nematic liquid crystals. *Europhys Lett* 72(3):403–409.
28. Tasinkevych M, Silvestre NM, Telo da Gama MM (2012) Liquid crystal boojum-colloids. *New J Phys* 14:073030.
29. Liu Q, Senyuk B, Tasinkevych M, Smalyukh II (2013) Nematic liquid crystal boojums with handles on colloidal handlebodies. *Proc Natl Acad Sci USA* 110(23):9231–9236.
30. Wood TA, Lintuvuori JS, Schofield AB, Marenduzzo D, Poon WCK (2011) A self-quenched defect glass in a colloid-nematic liquid crystal composite. *Science* 334(6052):79–83.
31. Cantarella J, Kusner RB, Sullivan JM (2002) On the minimum ropelength of knots and links. *Inventiones Mathematicae* 150(2):257–286.
32. Martinez A, Mireles HC, Smalyukh II (2011) Large-area optoelastic manipulation of colloidal particles in liquid crystals using photoresponsive molecular surface monolayers. *Proc Natl Acad Sci USA* 108(52):20891–20896.
33. Nelson DR (2002) Toward a tetravalent chemistry of colloids. *Nano Lett* 2(10):1125–1129.
34. Kleman M (1977) Relationship between burgers circuit, volterra process and homotopy groups. *J. de Physique Letters* 38:L199–L202.
35. Bouligand Y (1974) Recherches sur les textures desetats mesomorphes. Dislocations coins et signication des cloisons de grandjean-cano dans les cholesteriques. *J Phys (Paris)* 35:959–981.
36. Machon T, Alexander GP (2013) Knots and nonorientable surfaces in chiral nematics. *Proc Natl Acad Sci USA* 110(35):14174–14179.
37. Jampani VSR, et al. (2011) Colloidal entanglement in highly twisted chiral nematic colloids: Twisted loops, Hopf links, and trefoil knots. *Phys Rev E Stat Nonlin Soft Matter Phys* 84(3 Pt 1):031703.